

# Multiple image deblurring with high dynamic-range Poisson data

Marco Prato, Andrea La Camera, Carmelo Arcidiacono, Patrizia Boccacci, and Mario Bertero

## 1 Introduction

Image deconvolution is a classical inverse and ill-posed problem which was investigated since the dawn of regularization theory. Nowadays there exists a plethora of methods and also some good codes for its solution. Examples for astronomical applications are provided by IDAC [34], MISTRAL [38] and AIDA [33]. In these codes a weighted least-squares approximation to the Poisson data fidelity function is used. This approximation is justified by the fact that data are perturbed by both Poisson and Gaussian noise, and, when the number of counts is large, a Poisson distribution can be approximated by a Gaussian one (for a discussion see [49]).

Therefore the question is: why to propose other methods? The answer is that, as far as we know, all regularized deconvolution methods do not produce satisfactory reconstructions in the case of images with high dynamic range, i.e. images where extremely bright and localized sources are superimposed to fainter and smoothly varying structures. In general the reconstructions are affected by significant ringing artifacts around the bright sources.

In this paper we propose methods for dealing with this difficulty in the framework of multiple deconvolution of images satisfying Poisson statistics. This problem arises, for instance, in the case of images obtained by Fizeau interferometry [8], a particular feature of the Large Binocular Telescope (LBT) [31]. Of the two Fizeau

---

Marco Prato

Dipartimento di Scienze Fisiche, Informatiche e Matematiche, Università di Modena e Reggio Emilia, Via Campi 213/b, 41125 Modena, Italy, e-mail: marco.prato@unimore.it

Andrea La Camera, Patrizia Boccacci, and Mario Bertero

Dipartimento di Informatica, Bioingegneria, Robotica e Ingegneria dei Sistemi (DIB-RIS), Università di Genova, Via Dodecaneso 35, 16145 Genova, Italy, e-mail: andrea.lacamera@unige.it, patrizia.boccacci@unige.it, bertero@disi.unige.it

Carmelo Arcidiacono

Osservatorio Astronomico di Padova, Istituto Nazionale di Astrofisica, vicolo dell'Osservatorio 5, 35122 Padova, Italy, e-mail: carmelo.arcidiacono@inaf.it

interferometers planned for this unique telescope, one, the so-called LBTI [32], has already produced the first interferometric images [37, 21], while the other, LINC-NIRVANA [29], is currently being commissioned and routinely performs Adaptive Optics observations at LBT Observatory [30]. Our group participated in the deconvolution of the first images of LBTI, showing, for the first time, the possibility of resolving volcanic structures on the surface of the Jovian moon Io from ground based observations [21].

Since we need efficient regularized methods, we first describe the application of the Scaled Gradient Projection (SGP) method to the regularized deconvolution of Poisson data. SGP is a general optimization method for the minimization of differentiable objective functions as proposed in [16]; therefore it can be used when the data fidelity function of Poisson data is regularized with the addition of a differentiable function. As concerns the choice of the scaling, we derive it from the Split-Gradient Method (SGM) proposed in [36]. This algorithm, with different kinds of regularization is already implemented in the software package AIRY<sup>1</sup> [23, 19].

For the deconvolution of high dynamic range images we consider an approach proposed in [25, 28] which consists in assuming that the image to be reconstructed is the sum of two components: a point-wise one corresponding to the point bright sources (stars) and a smooth one representing the underlying structures. Moreover, a different regularization is used for the two components: a sparsity enforcing regularization in terms of  $\ell_1$  norm in pixel space for the point-wise component and a smoothing regularization for the other one. We call this approach a Multi-Component Method (MCM).

Since the  $\ell_1$  regularization of the point-wise component is unable to produce reconstructions which localize correctly the point sources, in a subsequent paper [35] we improve the MCM method in the particular case of a single star, with known position, surrounded by an unknown accretion disc. Thanks to the knowledge of the position of the star, in that paper we assume that the point-wise component consists of an array which is zero everywhere except in one given pixel (the star), a very strong constraint on this component; moreover simple  $\ell_2$  regularization is used for the smooth component and an alternating method is proposed for image reconstruction. This approach provides both a satisfactory estimate of the magnitude of the star and a satisfactory reconstruction of the accretion disc.

Having established the relevance of the knowledge of the location of the bright sources, in this paper we extend the approach by defining a suitable objective function where the unknowns are the intensities of the sources and the smooth component; next we consider the addition of a penalization term depending only on the smooth component; finally, by a suitable extension of SGP to this model, we propose a convergent iterative method for the minimization of this function with respect to the full set of variables,. Therefore only convex and differentiable regularizations of the smooth component are considered. Moreover, besides non-negativity, additional constraints such as the flux value of the complete science object (point-wise

---

<sup>1</sup> AIRY can be downloaded from <http://www.airyproject.eu>

plus smooth) can be introduced. The focus is on the case of interferometric imaging, i.e. multiple image deconvolution.

Since, especially in the case of interferometric images, the localization of the bright sources can not be easily derived from the observed images, we also introduce an approach able to overcome this difficulty. We call it a Multi-Step Method (MSM). The first step consists in an SGP based deconvolution of the observed images and the result is used for estimating the localization of the bright sources. This allows to produce a mask which is used as an input of an MCM deconvolution; finally the result of this step is used as a background for a simple non-regularized SGP. The addition of the result of this step to that of the previous one produces the final reconstruction.

In conclusion, the main contributions of our paper are the following:

- The extension of SGP to the regularized deconvolution of multiple images of the same target, with specific applications to Fizeau interferometric images; in addition, differentiable edge-preserving regularization functions, introduced in the existing literature, are considered and discussed.
- Introduction of the multi-component model derived from our approach to the deconvolution of multiple images of targets containing bright spots superimposed to smooth and unknown structures.
- Extension of SGP to the minimization of the objective function derived from the previous model.
- Proposal of MSM for the practical application of the multi-component model to the case of interferometric images. The first step provides an estimate of the localization of the bright sources thanks to a standard SGP deconvolution.

The paper is organized as follows. In Sect. 2 we describe the regularization methods for multiple image deconvolution and we briefly discuss the choice of the parameters appearing in these methods. In Sect. 3 we give the SGP algorithm for multiple image deconvolution both in the standard case and in the case of boundary effect correction; the latter is based on an approach proposed in [6] for single image and in [1] for multiple image deconvolution. Sect. 4 is devoted to the problem of the reconstruction of high-dynamic images. In Sect. 4.1 we introduce our model based on the knowledge of the location of the bright sources and we propose the appropriate objective function and the corresponding SGP method for its minimization while in Sect. 4.2 we describe the approach based on MSM for the case of interferometric imaging. In Sect. 5 we demonstrate the accuracy provided by these methods by deconvolving both simulated and real images of Io observed in M-band with LBTI [37, 21]. Indeed these images are characterized by bright spots, due to volcanic activity, superimposed to the smooth surface of the moon. We also discuss the possibility of performing photometric analysis on the deconvolved images provided by MSM. Finally in Sect. 6 we summarize the results achieved with our approaches.

All methods are implemented in IDL and the codes are available to the users both in AIRY and in the stand-alone package contained in OASIS <sup>2</sup>.

---

<sup>2</sup> <http://www.oasis.unimore.it/site/home/software.html>

## 2 The regularization methods

In the case of Poisson data, the data-fidelity function is given by the sum of the Csiszár I-divergences [48, 24], also called generalized Kullback-Leibler divergences or cross-entropies, between the  $p$  detected and the corresponding computed images

$$J_0(f; g) = \sum_{j=1}^p \sum_{m \in S} \left\{ g_j(m) \ln \frac{g_j(m)}{(A_j f)(m) + b_j(m)} + (A_j f)(m) + b_j(m) - g_j(m) \right\}, \quad (1)$$

where  $m$  is a multi-index varying on the pixels of the image and object domain  $S$ ; the detected images  $g_j$ , ( $j = 1, \dots, p$ ) correspond to the same science object  $f$ ; the backgrounds  $b_j$  are the known expected values of the sky emission and  $A_j$  the known imaging matrices given by  $A_j f = K_j * f$ ; here  $K_j$  is the point spread function (PSF) of the  $j$ -th image and  $*$  denotes convolution product. In general the PSFs are normalized to unit flux. If  $p > 1$ , then the problem we have in mind is that of  $p$  different Fizeau interferometric images obtained with different orientations of the baseline [8]. Except for constants, which do not influence the minimizers,  $J_0(f; g)$  is the negative logarithm of the likelihood.

A regularization of the data fidelity function can be derived from a Bayesian approach; in such a way the negative logarithm of the posterior probability distribution is a function with the following structure [36, 27, 7]

$$J_\beta(f; g) = J_0(f; g) + \beta J_1(f), \quad (2)$$

where the regularization function  $J_1(f)$  derives from the negative logarithm of a Gibbs prior assumed for the unknown solution and the positive parameter  $\beta$  plays the role of a regularization parameter. Then the Maximum A Posteriori (MAP) estimates of the science object  $f$  are the solutions of the minimization problem

$$f_\beta = \arg \min_{f \in \Omega} J_\beta(f; g), \quad (3)$$

where  $\Omega$  is either the non-negative orthant or the set of the non-negative arrays such that

$$\sum_{n \in S} f(n) = c, \quad c = \frac{1}{p} \sum_{j=1}^p \sum_{m \in S} [g_j(m) - b_j(m)], \quad (4)$$

$c$  being the mean flux of the background subtracted images.

We remark that the function  $J_0$  is non-negative and convex; therefore, if we consider regularizers with the same properties, these properties hold also for  $J_\beta$ . Moreover, some regularizers are strictly convex or the intersection of their null space with the null space of  $J_0$  contains only the null element. Then  $J_\beta$  is strictly convex and the MAP solution is unique [14].

The SGM algorithm [36] is based on a decomposition of the gradient of  $J_1$  with the following structure

$$-\nabla J_1(f) = U_1(f) - V_1(f), \quad U_1(f), V_1(f) \geq 0, \quad (5)$$

where  $U_1, V_1$  are suitable non-negative arrays. Then, in its most simple form, it is given by

$$f^{(k+1)} = \frac{f^{(k)}}{p1 + \beta V_1(f^{(k)})} \circ \left( \sum_{j=1}^p A_j^T \frac{g_j}{A_j f^{(k)} + b_j} + \beta U_1(f^{(k)}) \right), \quad (6)$$

where  $A_j^T$  is the transposed matrix,  $x \circ y$  denotes the pixel by pixel product of two arrays and the quotient symbol denotes their pixel by pixel quotient. The algorithm reduces to the Richardson-Lucy (RL) algorithm by setting  $\beta = 0$ . Although in principle any vector  $\nabla J_1(f)$  can be decomposed as in (5) (and the decomposition is not unique), there exist several widely used regularization terms for which this splitting follows straightly from the gradient expression [36].

In this paper we consider and implement in our software seven different regularization function: three classical Tikhonov regularizations, the cross entropy regularization and three edge-preserving regularizations: the Hypersurface (HS) regularization, the Markov Random Field (MRF) regularization and the regularization function implemented in the MISTRAL code [38] which will be denoted as MIST. The last three functions contain an additional parameter  $\delta$ , which will be discussed at the end of this section. The expression of the seven regularization functions and the corresponding functions  $U_1, V_1$  are given in Appendix A.

An important issue in the use of regularization methods is the choice of the regularization parameter  $\beta$  which controls the balance between the two terms of  $J_\beta(f; g)$ . The choice of this parameter is an old problem widely discussed in the mathematical literature in the case of the regularization of the least-square problem. An account can be found, for instance, in [26, 5].

The case of Poisson noise was not so widely investigated. Criteria for the selection of  $\beta$  are proposed in [2, 9] and numerical simulations demonstrate that they work well when the number of counts is large. In the case of mixed Poisson and Gaussian noise (a noise model introduced for taking into account the read-out-noise in the case of images acquired by a CCD camera [46]), Gaussian noise can be approximated by a suitable Poisson noise in the way suggested in [47], and therefore the cited criteria can be applied also in this case.

However, simulations represent ideal cases. In the real world, when astronomical images are pre-processed for flat field correction, bad pixels removal, background subtraction etc., no rule is available because the pre-processing modifies the statistical properties of the noise. Therefore one can only attempt reconstructions with different values of  $\beta$  using some rules for estimating at least its order of magnitude. It is only possible to say that for the observation of a given science object the value of  $\beta$  depends on the noise level, hence on the integration time: if the integration time increases, then the appropriate value of  $\beta$  decreases.

In the case of images affected by Poisson noise the value of  $J_0$  is approximately independent of  $g$  (for sufficiently large number of counts) if  $f$  is close to the correct solution; more precisely its value is of the order of  $N^2/2$  (see, for instance, [8]).

This rule is not satisfied if the images have been pre-processed, but it may give the order of magnitude of the first term in the regularized functional, except when the images are rescaled by the astronomers. Since  $J_0$  depends almost linearly on  $g$ , then the same rescaling can be done on its value. The estimated value of  $J_0$  provides a hint on the order of magnitude of  $\beta$  if one can estimate the order of magnitude of  $J_1$  by taking into account parameters deduced from the detected images such as the mean of the pixel values or the mean of the gradient values. Since  $\beta$  provides a balance between the two terms of  $J_\beta$ , then one can do a search around the value of  $\beta$  provided by the quotient  $J_0/J_1$  and look for a solution which could be the best for his purposes.

In addition to  $\beta$  the three edge-preserving regularization functions considered in this paper, namely HS, MRF and MIST defined in the Appendix, contain the additional parameter  $\delta$ . For simplicity we discuss mainly the case of HS regularization, defined in (36), where  $\delta$  clearly plays the role of a threshold for the values of the modulus of the gradient of the science object (defined as  $|D|$  in (28)). Therefore, the role of this parameter is very important.

Indeed, when  $\delta$  is small with respect to  $|D|$ , the above-mentioned regularizer behaves essentially as Total Variation (TV) regularization. This point has been demonstrated numerically in [15]. It is obvious that in such a case, since HS is differentiable, one can use very efficient optimization methods and obtain the same results provided by TV with a much lower computational cost. On the other hand, when  $\delta$  is greater than  $|D|$ , the regularizer behaves essentially as a Tikhonov regularization, based on the  $\ell_2$  norm of the gradient (see (31)). This result follows by a first-order Taylor expansion with respect to  $|D|/\delta$ . Therefore HS behaves as a sort of interpolation between TV and T-2 regularization and may be free of the undesirable cartoon effects due to TV regularization.

The point is to find a good value of  $\delta$ , i.e. a good thresholding separating regions with small values of the gradient and regions with high values of the gradient. In practice, since the values of the gradient of the unknown science object are also unknown, for estimating a suitable value of  $\delta$  one can first compute the mean value  $\delta_{\text{mean}}$  of the modulus of the gradient on the observed image; next perform a search of  $\delta$  around this mean value in order to find the best value for the user. In such a case, HS regularization behaves essentially as a T-2 regularization in regions where the gradient is smaller than  $\delta_{\text{mean}}$  but behaves as an edge-preserving regularization in regions where the gradient is very large (for instance, in the neighborhood of jumps in the values of the scientific target, as those due to the limb of a planet). In these cases HS provide an improvement with respect to TV since it does not introduce cartoon effects in the smooth regions.

For the deconvolution of images with a moderate dynamic range it may be convenient to take a value of  $\delta$  slightly higher than  $\delta_{\text{mean}}$ , because of the smoothing effect due to the PSF. On the other hand in the deconvolution of images with very high dynamic range, based on the multi components approach described in the following, it is convenient to take a value of  $\delta$  smaller than  $\delta_{\text{mean}}$  for the reconstruction of the smooth component, because  $\delta_{\text{mean}}$  is affected by the contribution of the bright

and localized sources. We take into account this effect in the case of our numerical simulations as well as in the reconstruction of real images.

### 3 The scaled gradient projection method

The convergence of SGM is not guaranteed unless some further sufficient decrease strategies are introduced [36]. Moreover, it is known that the convergence speed is slow.

Starting from the remark that SGM can be written as a scaled gradient method with fixed unitary step-length, i.e.,

$$f^{(k+1)} = f^{(k)} - \frac{f^{(k)}}{p1 + \beta V_1(f^{(k)})} \circ \nabla J_\beta(f^{(k)}; g) , \quad (7)$$

the SGP method [16] is a natural way to accelerate SGM by introducing variable step-lengths and projections.

In its general form, SGP can be applied to the minimization of any smooth objective function subject to a feasible set  $\Omega$  on which the projection is fast to compute, as in the case of box (possibly with the addition of an equality) constraint. Feasibility of the iterations and stationarity of the limit points of the sequence are achieved by a projection on the constraints  $P_\Omega$  and a line-search parameter  $\lambda_k$  automatically detected by means of a monotone Armijo backtracking rule [10], thus resulting in the iteration

$$f^{(k+1)} = f^{(k)} + \lambda_k \left( P_\Omega(f^{(k)} - \alpha_k D_k \circ \nabla J_\beta(f^{(k)}; g)) - f^{(k)} \right), \quad (8)$$

where

$$D_k = \min \left[ L_2, \max \left\{ L_1, \frac{f^{(k)}}{p1 + \beta V_1(f^{(k)})} \right\} \right] \quad (9)$$

and

$$P_\Omega(y^{(k)}) \equiv \arg \min_{y \in \Omega} (y - y^{(k)})^T D_k^{-1} (y - y^{(k)}). \quad (10)$$

The choice of the step-length parameter  $\alpha_k$  is the one described e.g. in [41] and is based on the BB rules [3], even if any positive step-length can be exploited in the SGP scheme and generalizations with different strategies might be considered (see e.g. [39, 40]).

The SGP method has been used in both standard [41, 12, 50, 11] and blind [22, 42, 43] deconvolution of astronomical images as an effective accelerated RL algorithm. Under mild conditions on the thresholds  $L_1$ ,  $L_2$  of the scaling matrix  $D_k$ , the sequence generated by SGP converges linearly with respect to the objective function values [13], even if several numerical experiments show that the decrease of the objective function is comparable with state-of-the-art approaches for which quadratic convergence rate has been proved [39, 13].

The SGP method can be easily generalized to account for the boundary effect correction proposed in [6, 1] in the following way:

- extend the object  $f$  to a broader array  $\bar{S}$  containing the region  $R$  whose pixels contribute to the observed image defined on  $S \subset R$ ; if we denote by  $M_R$  (resp.  $M_S$ ) the arrays defined over  $\bar{S}$  which are 1 over  $R$  (resp.  $S$ ) and 0 outside, then set

$$\alpha_j(n) = \sum_{m \in \bar{S}} K_j(m-n) M_S(m) \quad , \quad n \in \bar{S} \quad ,$$

$$R = \{n \in \bar{S} \mid \alpha_j(n) \geq \sigma \quad \forall j = 1, \dots, p\} \quad ,$$

where  $\sigma > 0$  is a small quantity;

- extend the images  $g$  (resp. the backgrounds  $b$ ) to  $\bar{S}$  by zero padding (resp. defining  $b$  in  $\bar{S} \setminus S$  as constantly equal to the median value of the background radiation in  $S$ );
- define the scaling matrix  $D_k$  as

$$D_k = M_R \circ \min \left[ L_2, \max \left\{ L_1, \frac{f^{(k)}}{\alpha + \beta V_1(f^{(k)})} \right\} \right] \quad , \quad (11)$$

where  $\alpha(n) = \sum_{j=1}^p \alpha_j(n)$  ,  $n \in \bar{S}$ ;

- if the flux conservation is considered, substitute the constraint (4) with

$$\frac{1}{p} \sum_{n \in R} \alpha(n) f(n) = c \quad . \quad (12)$$

We have implemented SGP in IDL using all the regularization functions described in Appendix A, with or without boundary effect correction; the core is the implementation of the SGP algorithm described above.

The software allows the user to provide its own initialization  $f^{(0)}$ , otherwise a default constant  $N \times N$  image with pixel values equal to  $c/N^2$  is used. In the case of boundary effect correction, the default starting point is an image defined over  $\bar{S}$  as

$$f^{(0)}(m) = \begin{cases} (cp) / (\sum_{n \in R} \alpha(n)), & \text{if } m \in R \\ 0, & \text{if } m \in \bar{S} \setminus R \end{cases} \quad . \quad (13)$$

SGP iteration must be equipped with one or more stopping rules. In general, in the case of regularization, the iteration must be pushed to convergence. To this purpose we use the following stopping criterion, based on the decrease of the objective function

$$|J_\beta(f^{(k+1)}; g) - J_\beta(f^{(k)}; g)| \leq \nu J_\beta(f^{(k+1)}; g) \quad (14)$$

where  $\nu$  is a tolerance parameter.

## 4 High-dynamic range image deconvolution

In this section we describe our approaches to the problem of deconvolving images with a very high dynamic range.

### 4.1 The Multi-Component Method (MCM)

Deconvolving an image might be a particularly challenging problem when the object consists of very bright sources superimposed to diffuse structures, a common situation in astronomical imaging. Typical artifacts appearing in these cases consist in ringing artifacts around the bright sources, thus leading to an unsatisfactory reconstruction of the underlying diffuse structures and, possibly, also to inaccurate evaluation of the intensities of the bright sources.

A possible way to address this problem is to include this information in the model by assuming that the unknown target  $f$  is the sum of a point-wise component  $f_P$  and an extended and smooth one  $f_E$ , exploiting different regularization strategies for each component.

Since  $f_P$  is sparse one could use a sparsity enforcing regularization such as that provided by the  $\ell_1$  norm [25, 28]; however we prefer a much stronger regularization provided by information on the localization of the bright sources when this information can be derived from the observed images. As concerns  $f_E$  one can choose one of the regularizers described in Appendix A: for instance a Tikhonov regularizer if it is known that it is very smooth or an edge-preserving one if it contains edges such as the limb of a planet.

In [35] we consider this model by assuming that the positions of the bright sources are exactly known. We propose an iterative algorithm which, at each iteration, performs an RL iteration on the point-wise component (initialized with a mask which is 1 in the pixels of the sources and 0 elsewhere) and an SGM iteration, with T-0 regularization (see Appendix A for a definition), on the extended component. The specific application is the reconstruction of the jet emitted by a young star with known position. In this paper we assume that the sources are localized inside small regions so that one can construct a mask which is 1 on these regions and 0 elsewhere. No additional regularization is introduced for  $f_P$ .

For the application of SGP to this situation, namely known localizations of the bright sources, we define  $\mathbb{R}_{\geq 0}^{N \times N}$  as the set of  $N \times N$  matrices with non-negative entries and  $P$  as the prefixed sub-region of the  $N \times N$  region  $S$  where the bright sources are located; then the resulting minimization problem becomes

$$\min_{(f_E, f_P) \in \bar{\Omega}} J_{\beta}(f_E, f_P; g) \equiv J_0(f_E + f_P; g) + \beta J_1(f_E) , \quad (15)$$

where

$$\bar{\mathcal{Q}} = \{(f_E, f_P) \in \mathbb{R}_{\geq 0}^{N \times N} \times \mathbb{R}_{\geq 0}^{N \times N} \mid f_P(n) = 0 \forall n \in S \setminus P \text{ and } f = f_E + f_P \text{ satisfies (4)}\}. \quad (16)$$

As concerns implementation, the SGP algorithm is applied to a  $N \times N$  matrix  $f_E$  and a  $N_P$  vector  $f'_P$ , where  $N_P$  is the number of pixels in  $P$ , containing the values of  $f_P$  belonging to  $P$ . The user is asked to provide a  $N \times N$  mask  $M_P$  equal to 1 where the point sources are located and 0 elsewhere, from which a  $N_P$  vector of indexes  $i_P$  is automatically computed in order to track the position of the bright sources within the  $N \times N$  array.

The core of the IDL code is a unique SGP deconvolution step in which, given initializations  $f_E^{(0)}, f'_P{}^{(0)}$ , the two arrays are updated at each iteration according to Algorithm 1, where gradients and scaling matrices are computed according to the objective function in (15). This unique step is required if we wish to apply the flux constraint (4); however, deconvolution without this constraint is also possible.

In order to select the line-search parameter  $\lambda_k$  through the Armijo rule (see Step 5 of Algorithm 1), the current image  $f^{(k)}$  is computed by merging  $f'_P{}^{(k)}$  into a  $N \times N$  matrix  $f_P^{(k)}$  and computing the sum  $f^{(k)} = f_P^{(k)} + f_E^{(k)}$ . The bounds  $L_1, L_2$  for the scaling matrices are chosen separately for both components, while the step-length  $\alpha_k$  is computed through the “extended” gradient

$$\nabla J_\beta(f_E^{(k)}, f'_P{}^{(k)}; g) = [\mathcal{V}(\nabla_E J_\beta(f_E^{(k)}, f'_P{}^{(k)}; g)); \nabla'_P J_\beta(f_E^{(k)}, f'_P{}^{(k)}; g)], \quad (23)$$

being  $\nabla_E J_\beta$  (resp.  $\nabla'_P J_\beta$ ) the gradient of  $J_\beta$  with respect to the first  $N \times N$  (resp. last  $N_P$ ) variables,  $\mathcal{V}(h)$  the column vectorization of the array  $h$  and  $[h; h']$  the column vector obtained concatenating  $h$  and  $h'$ . The parameters  $\mu, \theta, \alpha_{\min}, \alpha_{\max}$  are the standard SGP ones (see e.g. [41]). As concerns the initializations, the fluxes of the point-wise objects in  $f'_P{}^{(0)}$  are chosen as those of the corresponding pixels of the background-subtracted observed image  $g_1$ . The remaining flux of the measured images (i.e., the value obtained by subtracting the flux of  $f'_P{}^{(0)}$  from the total flux  $c$  defined in (4)) is then spread on a constant  $N \times N$  matrix  $f_E^{(0)}$ , which represents the starting point for the extended object. However, the user can be freely insert his own initialization arrays.

If the boundary effect correction is included, the following modifications to the algorithm have to be considered:

- region  $S$  must be replaced by the  $N' \times N'$  region  $\bar{S}$  ( $N' > N$ );
- the set  $\bar{\mathcal{Q}}$  is defined as

$$\bar{\mathcal{Q}} = \{(f_E, f_P) \in \mathbb{R}_{\geq 0}^{N' \times N'} \times \mathbb{R}_{\geq 0}^{N' \times N'} \mid f_P(n) = 0 \forall n \in \bar{S} \setminus P \text{ and } f = f_E + f_P \text{ satisfies (12)}\}; \quad (24)$$

- the constant value of the pixels in  $f_E^{(0)}$  is computed according to the constraint (12);
- steps 1 and 3 of Algorithm 1 must be reformulated as follows:

STEP 1. Choose the parameter  $\alpha_k \in [\alpha_{\min}, \alpha_{\max}]$  and define the  $N' \times N'$  and  $N_P$  arrays

**Algorithm 1** Multi-component SGP

Choose the starting point  $(f_E^{(0)}, f_P^{(0)}) \in \bar{\Omega}$ , define the mask  $M_P$  and set the parameters  $\mu, \theta \in (0, 1)$ ,  $0 < L_1^E \leq L_2^E$ ,  $0 < L_1^P \leq L_2^P$ ,  $0 < \alpha_{\min} < \alpha_{\max}$ ,  $k_{\max} \in \mathbb{N}$ .

Extract the  $N_P$  vector  $f_P^{(0)}$  from  $f_P^{(0)}$  according to the entries  $i_P$  of mask  $M_P$  equal to 1.

Set  $k = 0$  and CHECK = TRUE.

While (CHECK = TRUE) and ( $k \leq k_{\max}$ ) do the following steps:

STEP 1. Choose the parameter  $\alpha_k \in [\alpha_{\min}, \alpha_{\max}]$  and define the  $N \times N$  and  $N_P$  arrays

$$D_k^E = \min \left[ L_2^E, \max \left\{ L_1^E, \frac{f_E^{(k)}}{p1 + \beta V_1(f_E^{(k)})} \right\} \right], \quad D_k^P = \min \left[ L_2^P, \max \left\{ L_1^P, \frac{f_P^{(k)}}{p1} \right\} \right]. \quad (17)$$

STEP 2. Compute the  $N \times N$  and  $N_P$  arrays

$$y_E^{(k)} = f_E^{(k)} - \alpha_k D_k^E \circ \nabla_E J_\beta(f_E^{(k)}, f_P^{(k)}; g), \quad y_P^{(k)} = f_P^{(k)} - \alpha_k D_k^P \circ \nabla_P J_\beta(f_E^{(k)}, f_P^{(k)}; g). \quad (18)$$

STEP 3. Compute the projection

$$\pi^{(k)} = P_\Omega([\mathcal{V}(y_E^{(k)}); y_P^{(k)}]), \quad (19)$$

where  $\Omega$  is the set of  $N^2 + N_P$  vectors of non-negative components possibly satisfying (4) and  $P_\Omega$  is defined in (10), re-size the first  $N^2$  components of  $\pi^{(k)}$  in a  $N \times N$  matrix  $\pi_E^{(k)}$  and define the  $N_P$  vector  $\pi_P^{(k)}$  equal to the last  $N_P$  components of  $\pi^{(k)}$ .

STEP 4. Compute the descent directions

$$d_E^{(k)} = \pi_E^{(k)} - f_E^{(k)}, \quad d_P^{(k)} = \pi_P^{(k)} - f_P^{(k)}. \quad (20)$$

STEP 5. Backtracking loop: compute the smallest positive integer  $m$  such that the inequality

$$J_\beta(f_E^{(k)} + \lambda_k d_E^{(k)}, f_P^{(k)} + \lambda_k d_P^{(k)}; g) \leq J_\beta(f_E^{(k)}, f_P^{(k)}; g) + \mu \lambda_k \nabla J_\beta(f_E^{(k)}, f_P^{(k)}; g) \cdot [\mathcal{V}(d_E^{(k)}); d_P^{(k)}] \quad (21)$$

is satisfied with  $\lambda_k = \theta^m$ .

STEP 6. Set

$$f_E^{(k+1)} = f_E^{(k)} + \lambda_k d_E^{(k)}, \quad f_P^{(k+1)} = f_P^{(k)} + \lambda_k d_P^{(k)} \quad (22)$$

and  $k = k + 1$ .

STEP 7. If the stopping criterion is satisfied, then set CHECK = FALSE.

End

Define  $f_P^{(k)}$  as a  $N \times N$  matrix of zeros with entries of indexes  $i_P$  equal to  $f_P^{(k)}$ .

$$D_k^E = M_R \circ \min \left[ L_2^E, \max \left\{ L_1^E, \frac{f_E^{(k)}}{\alpha + \beta V_1(f_E^{(k)})} \right\} \right], \quad (25)$$

$$D_k^P = \min \left[ L_2^P, \max \left\{ L_1^P, \frac{f_P^{(k)}}{\alpha} \right\} \right]. \quad (26)$$

STEP 3. Compute the projection

$$\pi^{(k)} = P_\Omega([\mathcal{V}(y_E^{(k)}); y_P^{(k)}]), \quad (27)$$

where  $\Omega$  is the set of  $N_R + N_P$  vectors (being  $N_R$  the number of pixels in  $R$ ) of non-negative components possibly satisfying (12) and  $P_\Omega$  is defined in (10), define  $\pi_E^{(k)}$  as a  $N' \times N'$  matrix of zeros with pixel values in  $R$  equal to the first  $N_R$  components of  $\pi^{(k)}$  and define the  $N_P$  vector  $\pi_P^{(k)}$  equal to the last  $N_P$  components of  $\pi^{(k)}$ .

## 4.2 The Multi-Step Method (MSM)

MCM, as described above, assumes that the positions of the bright point-wise sources are (at least approximately) known. This can be true in particular cases but not always, of course. In particular, in our recent attempts of improving the reconstruction of LBTI images [37, 21] we found that it should be important to know the positions of the bright spots corresponding to hot sources on the surface of Io, but these can not be derived from the interferometric images.

Therefore we developed an approach, which we call a Multi-Step Method (MSM) and we propose for the first time in this paper. It can be briefly described as follows and can be applied to both single- and multi-image deconvolution.

- Step 1 - Deconvolve the observed image (or images) with some algorithm, for instance SGP without regularization or with an edge-preserving regularization and a small value of  $\beta$ , for obtaining a sharpening of the image (and a removal of the interferometric fringes in the interferometric case).
- Step 2 - Determine the centroids of the bright regions which appear as a result of Step 1 and produce a mask which is one over the centroids, or small regions around the centroids, and zero elsewhere.
- Step 3 - Apply MCM to the observed image (images) using the previous mask and a regularizer which looks appropriate to the underlying structure. The output of this step is a reconstruction of this structure.
- Step 4 - If we denote as  $f_E$  the result of the previous step, then we write the unknown object as  $f = h + f_E$  and we can recover  $h$  by applying SGP, without regularization, to the observed images; thank to the fact that this algorithm concentrates the solution in a few regions, the result is a reconstruction of the bright sources, with possible artifacts consisting of a few bright pixels external to the domains of the sources. Also in this case the algorithm can be pushed to convergence. In alternative, one can use one of the available regularization algorithms, with a small value of the regularization parameter.

The final result is the sum of the results of Step 3 and Step 4. In the next section we will prove the efficacy of this approach to the reconstruction of Io images in M-band.

## 5 Numerical results

Because of our recent activity on LBTI images, in this section we focus on images of the Jovian moon Io in M-band. We mainly consider the application of MSM. In order to verify the accuracy of the reconstructions of the real images we generate simulated LBTI images at M-band [37, 21] of an Io-like object with SNR values comparable to those of the real ones. We select M-band images because in this case the hot spots, due to volcanic activity, are seen as very bright sources over the surface of the moon so that they produce very strong ringing artifacts in the case of standard deconvolution methods.

### 5.1 Simulated image

In this section we simulate an Io-like object with features similar to those of the M-band LBTI images of Io analysed in the next section. The size of all images is  $256 \times 256$ . As concerns the surface of the moon, we generate a disc with the same diameter of Io in the LBTI images and a smoothly variable brightness, including a sort of limb darkening, and we superimpose bright sources to it. To simulate a structure similar to that of Loki, the dominant structure in the observed LBTI images, we insert a set of three sources which can not be resolved by a 8m telescope. Moreover we use the PSFs provided with the LBTI images. The simulated surface and the simulated object, obtained by adding to the surface eleven hot, are shown in the first row of Fig. 1 while in the second row we show the PSF and the corresponding image in the case of horizontal baseline of the interferometer.

We first consider a set of four images with orientations of the baseline of 4, 49, 94 and 139 degrees, thus assuring a good coverage of the  $u, v$  plane. In the first step we use a number of iterations of SGP without regularization in order to sharpen the images of the nine hot spots. We compute the centroids of their reconstructions and we find that they coincide with the positions in the original model, except in one case where we find a shift of one pixel. These centroids are used for producing the mask (second step) to be used in the third step. In the third row of Fig. 1 (left panel) we show the result of the first step; it is evident that now the bright spots can be identified but they are encircled by strong ringing effects. In the right panel of the same row the mask obtained by this preliminary reconstruction is also shown.

Finally, in the third step, because of a sharp edge due to the limb of the planet, we decide to test only the three regularizers HS, MRF and MIST. For the three regularizers, we consider a grid of the two parameters  $\delta, \beta$  consisting of  $11 \times 9$  points, with  $\delta$  varying from  $10^{-1}$  to  $10^1$  (11 values) and  $\beta$  varying from  $10^{-3}$  to  $10^1$  (9 values). For each regularizer we consider SGP both with and without flux constraint. For each one of these six cases we find only one minimum of the r.m.s. error, computed as the  $\ell_2$  norm of the difference between the reconstructed and the original surface of the Io-like object.

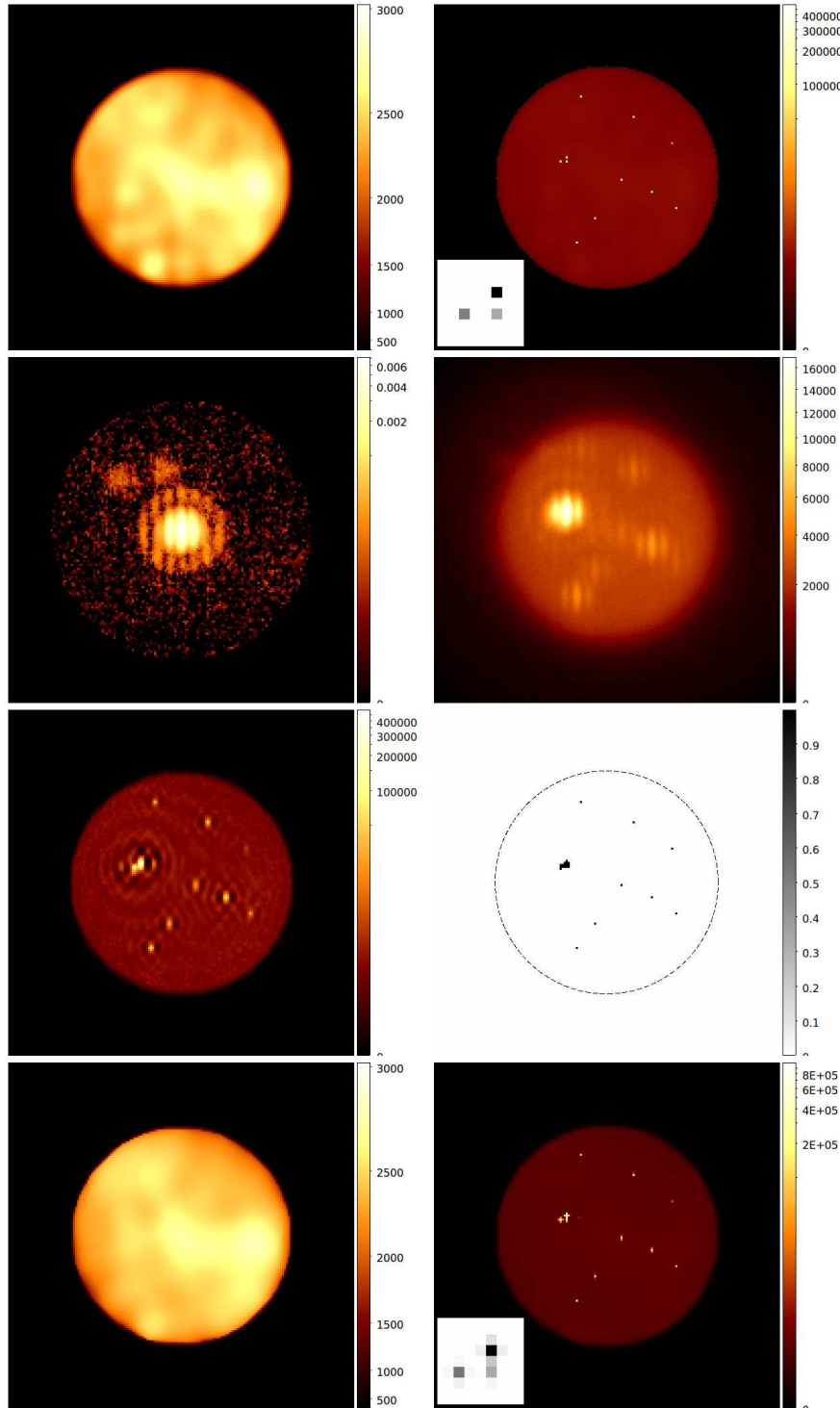


**Fig. 1** Simulated and reconstructed Io-like object in the case of complete coverage. *FIRST ROW* - *Left*: Model of the surface of the planet (quadratic scale). *Right*: The model after the addition of eleven hot spots (log scale with saturation of the hot spots). We visualize a zoom of the cluster of three spots in the lower left corner of the image. *SECOND ROW* - *Left*: The observed PSF (horizontal baseline), provided with the real images considered in the next section (log scale). *Right*: The corresponding noisy image. *THIRD ROW* - *Left*: The first step of the reconstruction obtained with non-regularized SGP. *Right*: The mask derived from the previous reconstruction. *FORTH ROW* - *Left*: The reconstructed surface. *Right*: The complete reconstruction (MRF regularization in the third step - see the text).

The best values of the parameters resulted  $\delta = 1$  and  $\beta = 10^{-1}$ . In the third step we use a tolerance of  $10^{-7}$  but we find that for resolving the Loki-like structure we need a tolerance of  $10^{-8}$  in the stopping criterion for the fourth step, corresponding to about 2500 iterations, a very large number for SGP. The reconstruction with minimal number of point-wise artifacts is obtained by MRF regularization with no flux constraint at the third step and flux constraint at the fourth one. The mean error on the reconstruction of the intensities of the hot points is about 2%. In the last row of Fig. 1 we show the reconstruction of the surface (left panel) and the complete reconstruction of the simulated Io-like object, including the eleven bright spots (right panel).

In a second experiment we consider a situation with a non-complete coverage of the  $u, v$  plane, similar to that of the LBTI observations considered in the next section. Therefore the orientations of the baseline correspond to -30, -22, -16, -8, 4, 16, 29 degrees [37]. We use the values of the parameters obtained from the first experiment. Also in this case it is possible to resolve the Loki-like structure with the same tolerances used in the previous experiment but now the required number of SGP iterations at the fourth step is much larger, about 4260.

## 5.2 Real image

We consider now the seven interferometric images of Io observed with LBTI during UT 2013 December 24. Observations and data reduction are described in [37]. After pre-processing the images contain negative values as a consequence of background subtraction. These negative values may cause troubles in algorithms which require non-negativity of the observed images. Therefore, instead of zeroing these values, which are small, we add a sufficiently large background such that the average value of the resulting one is not significantly affected by the negative values. We select, arbitrarily, a value of 100 which, of course, is also inserted in the reconstruction algorithm. Three of the observed images (after de-rotation for taking into account the rotation of the baseline with respect to the moon) are shown in the upper panels of Fig. 2. A PSF is also provided, derived from the image of the star HD-78141 and already shown in Fig. 1. During the observation time of about 1 hour the Io relative orbital rotation is of  $7.7^\circ$ . Therefore in the reconstruction of these images we have two additional difficulties: an approximate PSF and a variation of the target during the observation time. We ignore these difficulties in the subsequent analysis.

For the reconstruction of these images we use MRF regularization in the third step. As concerns the values of the parameters  $\beta$ ,  $\delta$ , inspired by the reconstruction of the simulated images with similar SNR values, we considered three values of  $\delta$  from 0.1 to 1 ( $\delta_{\text{mean}} = 1.6$ ) and six values of  $\beta$  from 0.1 to 0.01., with tolerance  $10^{-7}$  for stopping the iteration. By looking at the reconstruction of the surface of the moon, we decided to consider two cases, both with  $\delta = 1$ :  $\beta = 5 \times 10^{-2}$  and  $\beta = 10^{-2}$ . The corresponding results obtained in the last step by using SGP without regularization are shown respectively in the second and third row of Fig. 2. The

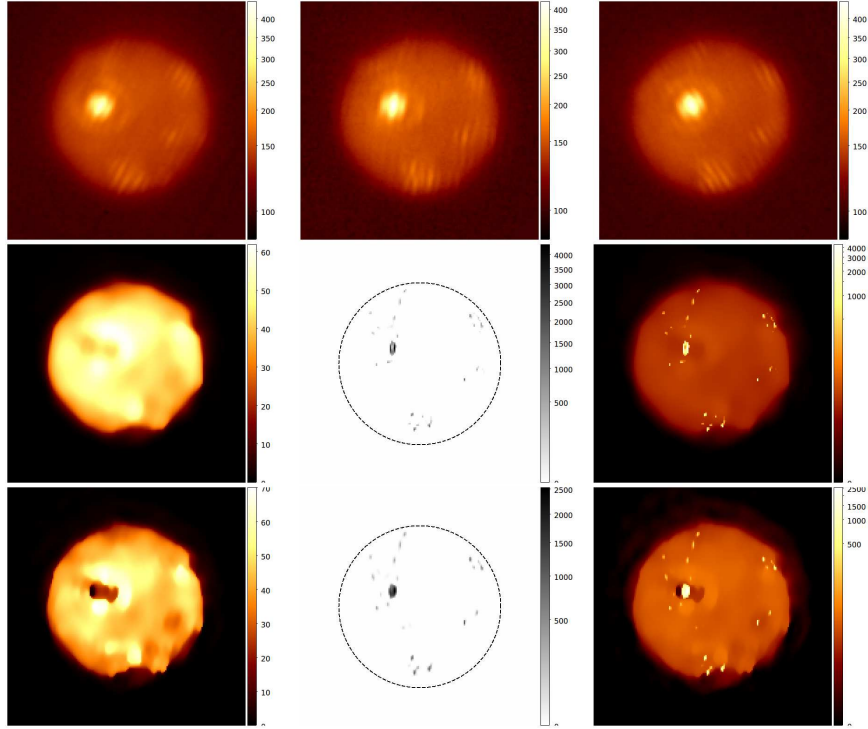


**Fig. 2** Reconstruction of the LBTI images of Io at M-band. *FIRST ROW* - Three interferometric images, showing the variation of the parallactic angle of about  $60^\circ$ . *SECOND ROW* - *Left*: The reconstructed surface of Io (linear scale) as obtained at the 3rd step with MRF regularization,  $\delta = 1$  and  $\beta = 5 \times 10^{-2}$ . *Middle*: The reconstruction of the hot spots, in reverse gray sqrt scale (the limb is identified with a dashed circle). *Right*: The complete reconstruction: surface plus hot spots (log scale). *THIRD ROW* - Same as in the second row but with  $\beta = 10^{-2}$ .

number of iterations for the last step is 331 in the first case and 113 in the second one.

A general comment is that the reconstruction of the limb is very irregular. This fact is due to two effects: the existence of hot spots close to the limb and a variation of the position of Io inside the image, since the images are centered on Loki, the brightest structure visible in them. A second comment is that the use of a too small regularization parameter does not remove completely ringing artifacts around Loki even if it is able to reduce the point-wise artifacts.

As concerns the eruptions visible in these reconstructions, we do not find evidence for those of Gibil and Rarog (see [21]), even if they were introduced into our mask, consisting of domains of  $3 \times 3$  pixels for each assumed hot spot (and a broader domain for Loki); we do not exclude their existence but they are certainly very faint so that it is difficult to detect their existence over an estimated and certainly approxi-

mated background. Anyway their existence was deduced from reconstructed images full of artifacts.

On the other hand we find two hot spots close to Loki, respectively above right and below left, not considered in the previous reconstructions. If we look at the local reconstructions of Loki, used in [21] and represented in log scale, we find two faint shadows in the same locations; therefore the two hot spots are presumably deriving from these two shadows, as an effect of the last step since non-regularized SGP tends to concentrate the flux in small regions; we also point out that they are stronger in the reconstruction of the second row of Fig. 2 and fainter in that to the third row. Therefore they can be artifacts due to the approximate PSF and the deconvolution method. We must also remark that Loki is so bright that its reconstruction can easily generate artifacts in the deconvolved images. We also observe that Loki is resolved in the reconstruction of the second row but not in that to the third one.

Finally, as concerns photometry, we remark that the eruptions are very well localized in the reconstruction shown in the third row. Since an estimate of the flux of Loki is given in [21], by means of these reconstructions it is easy to compute the ratio between the intensity of one eruption and that of Loki, thus obtaining its flux.

## 6 Concluding remarks

In this paper we first discuss the application of SGP to the regularized inversion of Poisson data. Thanks to its efficiency and flexibility, it can be easily used in complex methods we propose for the deconvolution of images with a very high dynamic range. All the methods are implemented in IDL and are at disposal of the reader.

We test the methods for high-dynamic range deconvolution on simulated and real images of the Jovian moon Io. As concerns the real images, we consider LBTI images of a Loki eruption. We show that they provide reconstructions which are free of the usual ringing artifacts even if another kind of artifacts, consisting in a small number of not very bright pixels, is introduced. Anyway these artifacts are not disturbing too much so that it seems that they do not prevent a photometric analysis of the reconstructed images. This point should be very important; however it requires a further and more detailed analysis.

**Acknowledgements** We thank Al Conrad, LBTO<sup>3</sup>, for permission of using images of Io at M-band, observed with LBTI/LMIRcam [32, 45] during UT 2013 December 24 [37, 21]. Marco Prato is a member of the INdAM Research group GNCS, which is kindly acknowledged.

---

<sup>3</sup> The LBT is an international collaboration among institutions in the United States, Italy and Germany. LBT Corporation partners are: The University of Arizona on behalf of the Arizona Board of Regents; Istituto Nazionale di Astrofisica, Italy; LBT Beteiligungsgesellschaft, Germany, representing the Max-Planck Society, the Leibniz Institute for Astrophysics Potsdam, and Heidelberg University; the Ohio State University, and the Research Corporation, on behalf of the University of Notre Dame, University of Minnesota and University of Virginia.

## Appendix

### Regularization functions

In this paper we assume that  $f$  is a  $N \times N$  array extended (when needed) with periodic boundary conditions, i.e., if we set  $n = (n_1, n_2)$ , then  $f(N+1, n_2) = f(1, n_2)$ ,  $f(n_1, N+1) = f(n_1, 1)$  and  $f(N+1, N+1) = f(1, 1)$ .

For introducing the regularization functions considered in our methods and software we need some notation. We set  $n_{1\pm} = (n_1 \pm 1, n_2)$  and  $n_{2\pm} = (n_1, n_2 \pm 1)$  and we introduce the square and the modulus of the discrete gradient

$$\begin{aligned} D^2(n) &= [f(n_{1+}) - f(n)]^2 + [f(n_{2+}) - f(n)]^2, \\ |D(n)| &= \sqrt{[f(n_{1+}) - f(n)]^2 + [f(n_{2+}) - f(n)]^2}. \end{aligned} \quad (28)$$

Then, the seven regularization functions and the corresponding arrays  $U_1, V_1$  are the following:

- **Zeroth order Tikhonov (T-0) regularization**

$$J_1(f) = \frac{1}{2} \sum_n |f(n)|^2, \quad (29)$$

for which (5) holds by setting

$$U_1(n) = 0, \quad V_1(n) = f(n). \quad (30)$$

- **First order Tikhonov (T-1) regularization**

$$J_1(f) = \frac{1}{2} \sum_n D^2(n), \quad (31)$$

for which (5) holds by setting

$$\begin{aligned} U_1(n) &= f(n_{1+}) + f(n_{2+}) + f(n_{1-}) + f(n_{2-}), \\ V_1(n) &= 4f(n). \end{aligned}$$

- **Second order Tikhonov (T-2) regularization**

$$J_1(f) = \frac{1}{2} \sum_n (\Delta f)(n)^2, \quad (32)$$

where  $\Delta$  denotes the discrete Laplacian. As remarked in [36], it can be written in the form

$$J_1(f) = \frac{1}{2} \sum_n [f(n) - (Bf)(n)]^2, \quad (33)$$

where  $B$  is the convolution matrix obtained from the  $3 \times 3$  mask with columns  $(0, 1/4, 0)$ ,  $(1/4, 0, 1/4)$  and  $(0, 1/4, 0)$ . Then (5) holds by setting

$$\begin{aligned} U_1(n) &= [(B + B^T)f](n) , \\ V_1(n) &= [(I + B^T B)f](n) . \end{aligned}$$

- **Cross-Entropy (CE) regularization** [17, 18]

$$J_1(f) = KL(f, \bar{f}) = \sum_n \left\{ f(n) \ln \left( \frac{f(n)}{\bar{f}(n)} \right) + \bar{f}(n) - f(n) \right\} , \quad (34)$$

where  $\bar{f}$  is a reference image. When  $\bar{f}$  is a constant array, then the cross-entropy becomes the negative Shannon entropy considered, for instance, in [44]. If both  $f$  and  $\bar{f}$  satisfy the constraint (4), then a possible choice for the functions  $U_1$ ,  $V_1$  is

$$U_1(n) = -\ln \frac{f(n)}{c} , \quad V_1(n) = -\ln \frac{\bar{f}(n)}{c} , \quad (35)$$

where  $c$  is the flux constant defined in (4). We remark that, since the background is taken into account by the algorithms,  $f$  can be zero in some pixels; for this reason in the computation of the gradient we add a small quantity to the values of  $f$ . We also remark that when  $\bar{f}$  is a constant, e.g.  $c/N^2$ , then  $V_1(n) = 2 \ln N$ .

- **Hypersurface (HS) regularization** [20]

$$J_1(f) = \sum_n \sqrt{\delta^2 + D^2(n)} , \quad \delta > 0 , \quad (36)$$

for which (5) holds by setting

$$\begin{aligned} U_1(n) &= \frac{f(n_{1+}) + f(n_{2+})}{\sqrt{\delta^2 + D^2(n)}} + \frac{f(n_{1-})}{\sqrt{\delta^2 + D^2(n_{1-})}} + \frac{f(n_{2-})}{\sqrt{\delta^2 + D^2(n_{2-})}} , \\ V_1(n) &= \frac{2f(n)}{\sqrt{\delta^2 + D^2(n)}} + \frac{f(n)}{\sqrt{\delta^2 + D^2(n_{1-})}} + \frac{f(n)}{\sqrt{\delta^2 + D^2(n_{2-})}} . \end{aligned}$$

The application of SGP to the case of HS regularization is already considered in [15] and [4] for a comparison of its accuracy with that of Total Variation (TV) regularization.

- **Markov random field (MRF) regularization** [27]

$$J_1(f) = \frac{1}{2} \sum_n \sum_{n' \in \mathcal{N}(n)} \sqrt{\delta^2 + \left( \frac{f(n) - f(n')}{\epsilon(n')} \right)^2} , \quad (37)$$

where  $\delta > 0$ ,  $\mathcal{N}(n)$  is a symmetric neighborhood made up of the eight first neighbors of  $n$  and  $\epsilon(n')$  is equal to 1 for the horizontal and vertical neighbors and equal to  $\sqrt{2}$  for the diagonal ones; thanks to the symmetry of  $\mathcal{N}(n)$ , Eq. (5) holds by setting

$$U_1(n) = \sum_{n' \in \mathcal{N}(n)} \frac{f(n')}{\epsilon(n') \sqrt{\delta^2 + \left(\frac{f(n') - f(n)}{\epsilon(n')}\right)^2}} ,$$

$$V_1(n) = \sum_{n' \in \mathcal{N}(n)} \frac{f(n)}{\epsilon(n') \sqrt{\delta^2 + \left(\frac{f(n) - f(n')}{\epsilon(n')}\right)^2}} .$$

• **MISTRAL regularization (MIST)** [38]

$$J_1(f) = \sum_n \left\{ |D(n)| - \delta \ln \left( 1 + \frac{|D(n)|}{\delta} \right) \right\} , \quad \delta > 0 , \quad (38)$$

for which (5) holds by setting

$$U_1(n) = \frac{f(n_{1+}) + f(n_{2+})}{\delta + |D(n)|} + \frac{f(n_{1-})}{\delta + |D(n_{1-})|} + \frac{f(n_{2-})}{\delta + |D(n_{2-})|} ,$$

$$V_1(n) = \frac{2f(n)}{\delta + |D(n)|} + \frac{f(n)}{\delta + |D(n_{1-})|} + \frac{f(n)}{\delta + |D(n_{2-})|} .$$

## References

1. Anconelli, B., Bertero, M., Boccacci, P., Carbillet, M., Lantéri, H.: Reduction of boundary effects in multiple image deconvolution with an application to LBT LINC-NIRVANA. *Astron. Astrophys.* **448**, 1217–1224 (2006)
2. Bardsley, J.M., Goldes, J.: Regularization parameter selection methods for ill-posed poisson maximum likelihood estimation. *Inverse Probl.* **25**, 095,005 (2009)
3. Barzilai, J., Borwein, J.M.: Two-point step size gradient methods. *IMA J. Numer. Anal.* **8**(1), 141–148 (1988)
4. Benfenati, A., Ruggiero, V.: Inexact bregman iteration with an application to poisson data reconstruction. *Inverse Probl.* **29**, 065,016 (2013)
5. Bertero, M., Boccacci, P.: *Introduction to Inverse problems in imaging*. IoP Publishing, Bristol (1998)
6. Bertero, M., Boccacci, P.: A simple method for the reduction of boundary effects in the Richardson-Lucy approach to image deconvolution. *Astron. Astrophys.* **437**, 369–374 (2005)
7. Bertero, M., Boccacci, P., Desiderà, G., Vicidomini, G.: Image deblurring with Poisson data: from cells to galaxies. *Inverse Probl.* **25**(12), 123,006 (2009)
8. Bertero, M., Boccacci, P., La Camera, A., Olivieri, C., Carbillet, M.: Imaging with LINC-NIRVANA, the Fizeau interferometer of the Large Binocular Telescope: state of the art and open problems. *Inverse Probl.* **27**(11), 113,011 (2011)
9. Bertero, M., Boccacci, P., Talenti, G., Zanella, R., Zanni, L.: A discrepancy principle for Poisson data. *Inverse Probl.* **26**(10), 10,500 (2010)
10. Bertsekas, D.: *Nonlinear programming*. Athena Scientific, Belmont (1999)
11. Bonettini, S., Landi, G., Loli Piccolomini, E., Zanni, L.: Scaling techniques for gradient projection-type methods in astronomical image deblurring. *Int. J. Comput. Math.* **90**(1), 9–29 (2013)
12. Bonettini, S., Prato, M.: Nonnegative image reconstruction from sparse Fourier data: a new deconvolution algorithm. *Inverse Probl.* **26**(9), 095,001 (2010)
13. Bonettini, S., Prato, M.: New convergence results for the scaled gradient projection method. *Inverse Probl.* **31**(9), 095,008 (2015)
14. Bonettini, S., Ruggiero, V.: On the uniqueness of the solution of image reconstruction problems with Poisson data. In: T.E. Simos, G. Psihoyios, C. Tsitouras (eds.) *International Conference of Numerical Analysis and Applied Mathematics 2010, AIP Conf. Proc.*, vol. 1281, pp. 1803–1806 (2010)

15. Bonettini, S., Ruggiero, V.: An alternating extragradient method for total variation-based image restoration. *Inverse Problems* **27**, 095,001 (2011)
16. Bonettini, S., Zanella, R., Zanni, L.: A scaled gradient projection method for constrained image deblurring. *Inverse Probl.* **25**(1), 015,002 (2009)
17. Byrne, C.L.: Iterative image reconstruction algorithms based on cross-entropy minimization. *IEEE Trans. Image Proc.* **2**(1), 96–103 (1993)
18. Carasso, A.S.: Linear and nonlinear image deblurring: a documented study. *SIAM J. Numer. Anal.* **36**(6), 1659–1689 (1999)
19. Carbillet, M., La Camera, A., Deguignet, J., Prato, M., Bertero, M., Aristidi, E., Boccacci, P.: Strehl-constrained reconstruction of post-adaptive optics data and the Software Package AIRY, v. 6.1. In: E. Marchetti, L.M. Close, J.P. Véran (eds.) *Adaptive Optics Systems IV, Proc. SPIE*, vol. 9148, p. 91484U (2014)
20. Charbonnier, P., Blanc-Féraud, L., Aubert, G., Barlaud, M.: Deterministic edge-preserving regularization in computed imaging. *IEEE T. Image Process.* **6**, 298–311 (1997)
21. Conrad, A., de Kleer, K., Leisenring, J., La Camera, A., Arcidiacono, C., Bertero, M., Boccacci, P., Defrère, D., de Pater, I., Hinz, P., Hofmann, K.H., Kürster, M., Rathbun, J., Schertl, D., Skemer, A., Skrutskie, M., Spencer, J., Veillet, C., Weigelt, G., Woodward, C.E.: Spatially Resolved M-Band Emission from Io’s Loki Patera-Fizeau Imaging at the 22.8m LBT. *Astron. J.* **149**(5), 1–9 (2015)
22. Cornelio, A., Porta, F., Prato, M.: A convergent least-squares regularized blind deconvolution approach. *Appl. Math. Comput.* **259**(12), 173–186 (2015)
23. Correia, S., Carbillet, M., Boccacci, P., Bertero, M., Fini, L.: Restoration of interferometric images: I. the software package AIRY. *Astron. Astrophys.* **387**, 733–743 (2002)
24. Csiszár, I.: Why least squares and maximum entropy? An axiomatic approach to inference for linear inverse problems. *Ann. Stat.* **19**(4), 2032–2066 (1991)
25. De Mol, C., Defrise, M.: Inverse imaging with mixed penalties. In: *Proc. Int. Symp. on Electromagnetic Theory (Pisa, Italy)*, pp. 798–800 (2004)
26. Engl, H.W., Hanke, M., Neubauer, A.: *Regularization of Inverse Problems*. Kluwer Academic Publishers, Dordrecht (1996)
27. Geman, S., Geman, D.: Stochastic relaxation, Gibbs distributions and the Bayesian restoration of images. *IEEE Trans. Pattern Anal. Mach. Intell.* **6**(6), 721–741 (1984)
28. Giovannelli, J.F., Coulais, A.: Positive deconvolution for superimposed extended source and point sources. *Astron. Astrophys.* **439**, 401–412 (2005)
29. Herbst, T., Ragazzoni, R., Andersen, D., Boehnhardt, H., Bizenberger, P., Eckart, A., Gaessler, W., Rix, H.W., Rohloff, R.R., Salinari, P., Soci, R., Straubmeier, C., Xu, W.: LINC-NIRVANA: a fizeau beam combiner for the large binocular telescope. In: W.A. Traub (ed.) *Interferometry for Optical Astronomy II, Proc. SPIE*, vol. 4838, pp. 456–465 (2003)
30. Herbst, T.M., Santhakumari, K.K.R., Klettke, M., Arcidiacono, C., Bergomi, M., Bertram, T., Berwein, J., Bizenberger, P., Briegel, F., Farinato, J., Marafatto, L., Mathar, R., McGurk, R., Ragazzoni, R., Viotto, V.: Commissioning multi-conjugate adaptive optics with LINC-NIRVANA on LBT. In: *Adaptive Optics Systems VI, Society of Photo-Optical Instrumentation Engineers (SPIE) Conference Series*, vol. 10703, p. 107030B (2018). DOI 10.1117/12.2313421
31. Hill, J.M., Green, R.F., Slagle, J.H.: The Large Binocular Telescope. In: *Ground-based and Airborne Telescopes, Proc. SPIE*, vol. 6267, p. 62670Y (2006)
32. Hinz, P., Bippert-Plymate, T., Breuninger, A., Connors, T., Duffy, B., Esposito, S., Hoffmann, W., Kim, J., Kraus, J., McMahon, T., Montoya, M., Nash, R., Durney, O., Solheid, E., Tozzi, A., Vaitheeswaran, V.: Status of the LBT interferometer. In: *Optical and Infrared Interferometry, Proc. SPIE*, vol. 7013, p. 701328 (2008)
33. Hom, E.F.Y., Marchis, F., Lee, T.K., Haase, S., Agard, D.A., Sedat, J.W.: Aida: an adaptive image deconvolution algorithm with application to multi-frame and three-dimensional data. *J. Opt. Soc. Am.* **A-24**, 1580–1600 (1994)
34. Jefferies, S.M., Christou, J.C.: Restoration of astronomical images by iterative blind deconvolution. *Astron. J.* **415**, 862–609 (1993)

35. La Camera, A., Antonucci, S., Bertero, M., Boccacci, P., Lorenzetti, D., Nisini, B.: Image reconstruction for observations with a high dynamic range: LINC-NIRVANA simulations of a stellar jet. In: F. Delplancke, F.J.K. Rajagopal, F. Malbet (eds.) *Optical and Infrared Interferometry III*, *Proc. SPIE*, vol. 8455, p. 84553D (2012)
36. Lantéri, H., Roche, M., Aime, C.: Penalized maximum likelihood image restoration with positivity constraints: multiplicative algorithms. *Inverse Probl.* **18**(5), 1397–1419 (2002)
37. Leisenring, J.M., Hinz, P.M., Skrutskie, M.F., Skemer, A., Woodward, C.E., Veillet, C., Arcidiacono, C., Bailey, V., Bertero, M., Boccacci, P., Conrad, A., de Kleer, K., de Pater, I., Defrère, D., Hill, J., Hofmann, K.H., Kaltenegger, L., La Camera, A., Nelson, M.J., Schertl, D., Spencer, J., Weigelt, G., Wilson, J.C.: Fizeau interferometric imaging of Io volcanism with LBTI/LMIRcam. In: *Optical and Infrared Interferometry IV*, *Proc. SPIE*, vol. 9146, p. 91462S (2014)
38. Mugnier, L.M., Fusco, T., Conan, J.M.: Mistral: a myopic edge-preserving image restoration method, with application to astronomical adaptive-optics-corrected long-exposure images. *J. Opt. Soc. Am. A* **21**(4), 1841–1854 (2004)
39. Porta, F., Prato, M., Zanni, L.: A new steplength selection for scaled gradient methods with application to image deblurring. *J. Sci. Comput.* **65**(3), 895–919 (2015)
40. Porta, F., Zanella, R., Zanghirati, G., Zanni, L.: Limited-memory scaled gradient projection methods for real-time image deconvolution in microscopy. *Commun. Nonlinear Sci. Numer. Simul.* **21**(1–3), 112–127 (2015)
41. Prato, M., Cavicchioli, R., Zanni, L., Boccacci, P., Bertero, M.: Efficient deconvolution methods for astronomical imaging: algorithms and IDL-GPU codes. *Astron. Astrophys.* **539**, A133 (2012)
42. Prato, M., La Camera, A., Bonettini, S., Bertero, M.: A convergent blind deconvolution method for post-adaptive-optics astronomical imaging. *Inverse Probl.* **29**(6), 065,017 (2013)
43. Prato, M., La Camera, A., Bonettini, S., Rebegoldi, S., Bertero, M., Boccacci, P.: A blind deconvolution method for ground based telescopes and fizeau interferometers. *New Astron.* **40**, 1–13 (2015)
44. Skilling, J., Bryan, R.K.: Maximum entropy image reconstruction: general algorithm. *Mon. Not. R. Astr. Soc.* **211**, 111–124 (1984)
45. Skrutskie, M.F., Jones, T., Hinz, P., Garnavich, P., Wilson, J., Nelson, M., Solheid, E., Durney, O., Hoffmann, W.F., Vaitheeswaran, V., McMahan, T., Leisenring, J., Wong, A., Garnavich, P., Wilson, J., Nelson, M., Sollheid, E., Durney, O., Hoffmann, W.F., Vaitheeswaran, V., McMahan, T., Leisenring, J., Wong, A.: The Large Binocular Telescope mid-infrared camera (LMIRcam): final design and status. In: I.S. McLean, S.K. Ramsay, H. Takami (eds.) *Ground-based and Airborne Instrumentation for Astronomy III*, *Proc. SPIE*, p. 77353H. *Proc. SPIE*, Vol. 7735 (2010). DOI 10.1117/12.857615. URL <http://proceedings.spiedigitallibrary.org/proceeding.aspx?articleid=750817>
46. Snyder, D.L., Hammoud, A.M., White, R.L.: Image recovery from data acquired with a charge-coupled-device camera. *J. Opt. Soc. Am. A* **10**(5), 1014–1023 (1994)
47. Snyder, D.L., Helstrom, C.W., Lanterman, A.D., Faisal, M., White, R.L.: Compensation for readout noise in CCD images. *J. Opt. Soc. Am. A* **12**(2), 272–283 (1995)
48. Titterton, D.: On the iterative image space reconstruction algorithm for ECT. *IEEE Trans. Med. Imaging* **6**(1), 52–56 (1987)
49. Vio, R., Bardsley, J., Wamsteher, W.: Least-squares methods with poissonian noise: Analysis and comparison with the richardson-lucy algorithm. *Astron. Astrophys.* **436**(2), 741–755 (2005)
50. Zanella, R., Boccacci, P., Zanni, L., Bertero, M.: Efficient gradient projection methods for edge-preserving removal of Poisson noise. *Inverse Probl.* **25**(4), 045,010 (2009)